Journal of Materials Science: Materials in Electronics (2019) 30:11327–11335
https://doi.org/10.1007/s10854-019-01480-0

Transparent nanoporous P-type NiO films grown directly on non-native substrates by anodization

Ryan Kisslinger[1] · Saralyn Riddell[1] · Spencer Savela[1] · Piyush Kar[1] · Ujwal K. Thakur[1] · Sheng Zeng[1] · Karthik Shankar[1]

Received: 17 March 2019 / Accepted: 6 May 2019 / Published online: 14 May 2019

Abstract

While electrochemical anodization has been used to form a number of nanostructured *n*-type semiconducting metal oxides for optoelectronic device applications, there exists a dearth of *p*-type metal oxide films that are solution processable. Herein, we formed *p*-type semiconducting NiO films by vacuum depositing Ni thin films on non-native substrates (transparent conductive oxide (TCO)-coated glass substrates and silicon wafers) using magnetron sputtering, and subsequently anodizing and annealing the Ni films. The Ni films were subjected to electrochemical anodization in diethylene glycol based organic electrolytes and subsequently annealed at 600 °C to form nanoporous NiO films with a pore size of ~ 20 nm. Runaway etching is a key issue in Ni anodization which was mitigated through the use of ice bath cooling and galvanostatic anodization. The choice of substrate is found to be critical to the resulting morphology owing to the differing surface roughness. Crystalline NiO is found to have formed from $Ni(OH)_2$ and NiOOH during annealing, and an additional NiSi layer is noted for NiO films on Si wafers. The bandgap of the NiO was estimated to be 3.5 eV. Electrochemical impedance spectroscopy and Mott–Schottky analysis confirmed *p*-type semiconducting behaviour, and enabled measurement of an acceptor density (N_A) of 2.85×10^{18} cm^{-3} and a flatband potential (V_{FB}) of 0.687 V versus Ag/AgCl.

1 Introduction

Transparent semiconducting oxides are an important class of compounds for use as carrier transport layers or active layers in electronic applications such as solar cells, photocatalysts, transistors, sensors, and displays [1]. However, owing to the electronic configuration of oxides, the majority of available transparent semiconducting oxides are *n*-type as opposed to *p*-type; furthermore, available *n*-type transparent oxides deliver superior performance owing in part to their generally higher charge carrier mobilities [2]. Nanostructuring the oxide layer is particularly important in photodetectors, photocatalysts, photovoltaics and photoelectrochemical sensors to obtain high surface area electronic heterojunctions and to overcome the trade-off between light absorption and charge separation in light harvesting devices [3, 4]. Surface traps in nanostructured metal oxides are another important feature, and while traditionally viewed negatively, they have also been shown to be beneficial in photodetection, photocatalysis and sensing [5–7]. In *n*-type semiconducting oxides such as ZnO, TiO_2, Fe_2O_3, Ta_2O_5, Nb_2O_5 and WO_3, electrochemical anodization and solvothermal growth techniques have been used to achieve nanotube, nanopore and nanorod arrays with a high degree of control over the morphology of the metal oxide [8–20]. For *p*-type metal oxides, a similar degree of morphological control has been lacking. This has meant that many potential applications and device architectures are currently infeasible or impractical, and there is a need for new and improved *p*-type oxide materials. One possibility is NiO, which is a *p*-type oxide semiconductor that has been especially investigated for use in areas such as a transparent photocathode for photoelectrochemical systems [21] and as a hole transporting layer for perovskite solar cells [22]. Conventional methods to prepare NiO include evaporation, direct magnetron sputtering sol–gel techniques, and

Electronic supplementary material The online version of this article (https://doi.org/10.1007/s10854-019-01480-0) contains supplementary material, which is available to authorized users.

✉ Ryan Kisslinger
kissling@ualberta.ca

✉ Karthik Shankar
kshankar@ualberta.ca

[1] Department of Electrical and Computer Engineering, University of Alberta, 9211-116 St, Edmonton, AB T6G 1H9, Canada

electrodeposition [23, 24]. However, anodization of Ni to form nanostructured NiO remains largely unexplored, with only two previous reports on the topic [25, 26]. In each case, NiO was investigated for use as a *p*-type photocathode with the goal of conducting water splitting. Besides contributing to the generation of photocurrent, it is also hoped that NiO or similar *p*-type materials could replace the expensive platinum and gold counter electrodes that are typically used in photoelectrocatalytic systems.

Both previous studies resulted in a nanoporous nickel oxide, after anodization and annealing of a Ni foil. However, to the best of our knowledge there are no studies exploring the anodization of thin films of Ni on non-native substrates. This configuration is critical to the formation of a wide variety of real-world devices because such a substrate may either be a platform for integrating devices (e.g. silicon wafers), or may need to be transparent to allow for light to pass through for the function of optoelectronic devices (such as the case for glass coated with a transparent conductive oxide). Therefore, in this study, we have conducted electrochemical anodization on sputtered Ni films, which has resulted in nanoporous NiO. We further provide insight on the critical synthesis parameters during the sputtering and anodization processes, and performed material characterization to quantify some of the properties of the anodized films.

2 Experimental

2.1 Sample preparation

The substrates of fluorine-doped tin oxide (FTO)-coated glass, indium tin oxide (ITO)-coated glass, and <100> crystal axis, n^+-type, As-doped silicon wafers were used as-purchased from Hartford Glass Co., Guluo Glass and Kunshan Sino Silicon Technology Co. respectively. The FTO-coated glass had a sheet resistance of 8.2 ohms per square, the ITO-coated glass had a sheet resistance of 6.5 ohms per square, and the silicon wafer had a sheet resistance of 0.060 ohms per square. All pieces were cut to be approximately square with an area of about 5 cm^2 (referred to hereafter in this section as a "sample"). FTO-coated glass and ITO-coated glass were cleaned by sequential ultrasonication in acetone, methanol, and then deionized water for a duration of 10 min each before drying under a nitrogen stream. Silicon wafers were immersed in a piranha solution comprised of a 3:1 mixture of sulfuric acid and hydrogen peroxide for 15 min, followed by a buffered oxide etch comprised of a 10:1 mixture of ammonium fluoride and hydrofluoric acid, and then rinsed with deionized water. A section of FTO and ITO samples with an area of *ca.* 0.8 cm^2 was covered using Kapton tape to prevent metal deposition in this spot and allow for direct electrical contact to the substrate during anodization; the same was not done for Si wafers, and electrical contact was made directly to the backside of the Si wafer following scratching with a scriber. The sputter deposition of nickel was conducted for 10 min on all substrates in argon, with a power of 300 W, a deposition pressure of 4.5 mTorr, and substrate heating of 175 °C. The resulting film thickness was ~ 100 nm on top of the FTO or ITO coating. The Kapton tape was removed, and the exposed transparent conductive oxide attached via an affixed copper wire to a DC power supply. The sample was connected as the anode in an electrical circuit, with a 5 mm diameter graphite rod as the cathode. The anode and cathode were spaced 3 cm apart in a 30 mL beaker filled with the electrolyte; the electrolyte compositions used, the applied current/voltage, and the duration of the anodization process are discussed in a later section. After anodization, each sample was removed, soaked in methanol and deionized water for 1 min each, and dried under a nitrogen stream.

2.2 Characterization

Imaging of the anodized films was conducted using a Zeiss Sigma Field Emission Scanning Electron Microscope (FESEM). Pore size was determined from FESEM images by manually counting the diameter of 100 pores, and is reported as the mean value ± one standard deviation. X-ray diffraction (XRD) spectra were collected using a Rigaku Ultima IV equipped with a Cu-Kα source. Ultraviolet–visible (UV–Vis) spectroscopy was carried out using a Perkin Elmer Lambda 1050 Spectrophotometer equipped with a 100 mm integrating sphere. The sample was placed at the opposite end of the sphere from incoming light in front of a highly reflective Spectralon coating and diffuse reflectance was measured. X-ray photoelectron spectroscopy was conducted using an Axis-Ultra (Kratos Analytical) instrument equipped with a monochromatic Al-Kα source (15 kV, 50 W) under ultrahigh vacuum (~10^{-8} Torr). To adjust for charge correction, the spectra were adjusted so that the binding energy of the C 1 s core level of adventitious hydrocarbons matched the standard binding energy value of 284.8 eV.

2.3 Electrochemical impedance spectroscopy

Electrochemical impedance spectroscopy (EIS) was performed using a three-electrode configuration at an applied voltage of − 0.4 V vs the reference electrode Ag/AgCl in a pH 7, 0.1 M phosphate buffer solution comprised of 1 M K_2HPO_4 and 1 M KH_2PO_4 mixed together in a 61.5:38.5 volume ratio. Mott–Schottky plots were collected from impedance-potential measurements in the same 0.1 M phosphate buffer in the − 0.6 to + 1.6 V voltage range at 100 kHz frequency.

3 Results and discussion

3.1 Effect of synthesis parameters on anodized film morphology

The first step towards anodizing Ni thin films was the deposition of the film by sputtering. The key synthesis parameters selected here were inspired by the numerous studies conducted on anodizing Ti to form TiO_2 nanotubes, particularly on non-native substrates [27–40]. For example, it is understood that a denser metal substrate leads to a more well-defined and ordered porous morphology when anodizing Ti [25, 40, 41]. In the context of DC magnetron sputtering, film density is primarily controlled by the sputtering gas pressure and substrate temperature as is well-understood by the Thornton model [42, 43], where higher substrate temperatures and lower deposition pressures generally lead to a denser film. The sputtering system utilized here had a maximum achievable substrate temperature of 175 °c, so that was selected. The lowest possible argon gas pressure of 0.6 Pa was utilized to benefit from the atomic peening mechanism; we note that after experimentation with the sputtering system, it was found that any lower pressure would cause the plasma that is essential to the sputtering process to extinguish in this case, as not enough collisions to sustain the plasma.

The sputtered No thin films were anodized to result in a nanoporous nickel oxide film after annealing. This was accomplished by simultaneous electrochemical oxidation and etching processes during anodization. While etching processes are desired to allow for a porous structure, too fast an etching process would lead to complete removal of the films. An electrolyte comprised of 97 vol% diethylene glycol (DEG), 3 vol% deionized water, 0.15 M KOH, and 0.1 M NH_4F was found to produce the best porous structure; this is a modification of the recipe reported by Sápi et al [25], where we used DEG instead of ethylene glycol (EG). The importance of each component in the electrolyte is described as follows: first, in an anodization process to produce nanostructures, the electrolyte is often primarily composed of a polar organic solvent with a small amount of water. While organic electrolytes donate fewer O^{2-} ions at the electrolyte/oxide interface, thus leading to slower oxide growth, the etching of the oxide is also decreased, allowing for thicker, fully formed nanostructures [41, 44]. Thus, a small water content to supply some readily available O^{2-} ions is optimal. The use of DEG as the primary constituent of the anodization electrolyte increased the pore size from ~ 2–3 nm when using ethylene glycol (EG) to tens of nanometers—as can be directly compared between Fig. S1(a) and Fig. 1a which show the resultant morphology of EG and DEG-based anodization electrolytes respectively. The reason for the difference can be explained based on work conducted on large-diameter, widely spaced TiO_2 nanotubes using DEG-based electrolytes [45–49]. Due to the high viscosity of DEG and lower ionic mobilities in DEG, DEG-based electrolytes possesses a lower conductivity than EG-based electrolytes for similar concentrations of water and fluoride ions. Consequently, the much higher potential drop across the electrolyte results in low electric field conditions across the barrier layer and at the barrier layer-electrolyte interface, leading to a low population of nucleation sites [47–50]. In addition, field-assisted reactions responsible for oxide formation and etching are weaker, while chemical etching remains relatively unaffected. Since chemical etching is more isotropic than field assisted reactions, etching occurs more isotropically in DEG electrolytes, thus resulting in wider pores. In the case of nickel anodization, the resultant anodized material etches away too quickly in purely acidic solution to form a substantially thick nanostructured layer. The inclusion of KOH slows this process, to allow the morphology formed by the etching process to remain intact during anodization. We found that the temperature of the electrolyte is also important to the anodization process. Too high a temperature leads to a higher etching rate; as the etching process is itself exothermic, this can cause an avalanche effect and rampant etch rates; in this case, a nanoporous structure was not found (shown in Fig. S1(b)). For this reason, anodization was conducted with the anodization vessel contained within an ice bath. For a similar reason, we found that galvanostatic anodization is preferred over potentiostatic anodization for the formation of nanostructured nickel oxide. Upon applying a constant voltage, current densities initially decrease as an oxide layer is formed, followed by an increase owing to pitting caused by etching. However, if current densities become too high, we noticed a similar avalanche effect of etching rates and increasing temperature; the morphology of anodized nickel using a constant voltage process is shown in Fig. S1(c). It is noted that the morphologies displayed by constant voltage anodization in an ice bath and room temperature galvanostatic anodization display remarkable similarity.

SEM images of the anodized films using the optimized recipe are shown in Fig. 1. The imaged layers are labelled as NiO for FTO samples, $NiO_x(OH)_y$ on ITO samples, and NiO/NiSi for Si samples which is proven later. Clearly, there are significant differences in morphology between each substrate. The NiO formed on FTO resulted in small pores (13.4 ± 2.8 nm diameter), and etching occurred preferentially at grain boundaries. Meanwhile, the NiO formed on ITO and Si had larger pore diameters of 24.4 ± 7.4 nm and 22.7 ± 4.6 nm respectively. The ITO samples displayed much less preferential grain boundary

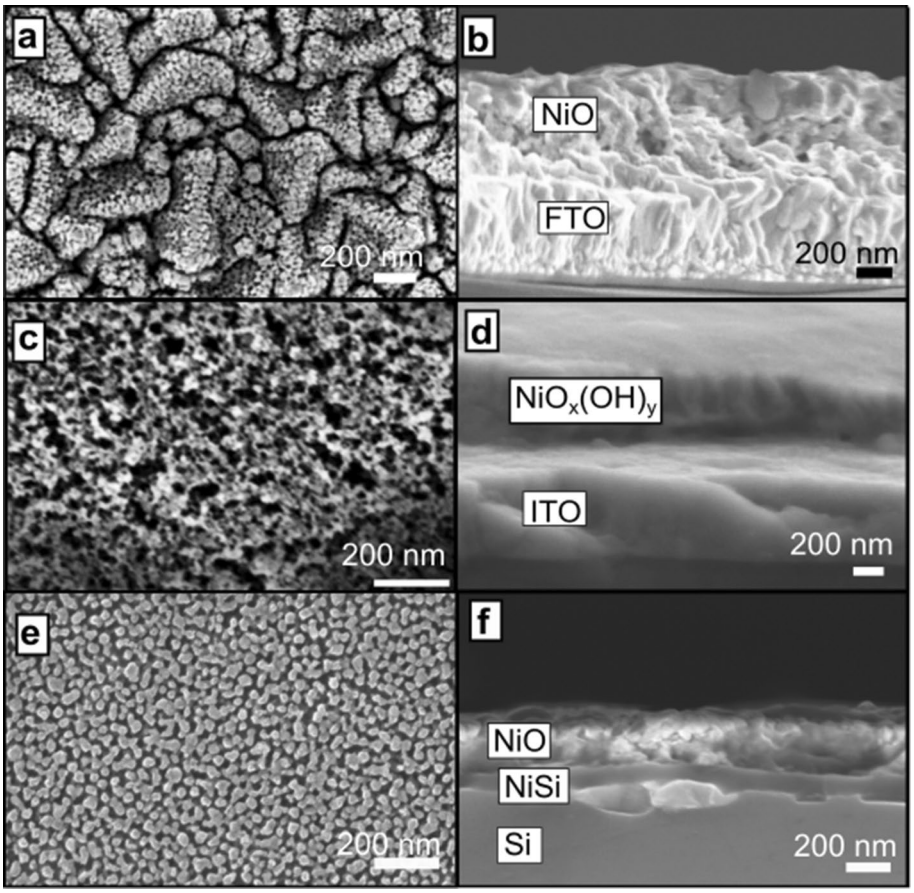

Fig. 1 Top view and cross-sectional SEM images of anodized Ni films on **a**, **b** FTO-coated glass, **c**, **d** ITO-coated glass, and **e**, **f** Si wafer. All scale bars correspond to 200 nm

etching than FTO samples, although the etched pores grew large enough to agglomerate in several locations; these locations resemble the structure of former grain boundaries, and it might be guessed that it is a small amount of preferential etching that caused this phenomenon. However, silicon samples displayed no preferential grain boundary etching. The primary reason for the difference in final NiO morphologies can be explained by the differing roughness of each substrate. As characterized by AFM (images of the AFM scans shown in Fig. S2), the root-mean-square roughness (S_q) of the sputtered Ni film on FTO glass, ITO glass, and the Si wafer was 28.8 nm, 5.58 nm, and 2.42 nm respectively. It follows that the rougher a film is, the more exposed grain boundaries there are. As grain boundaries are undergo chemical reactions at a higher rate than elsewhere in the film microstructure, the etching-pitting environment for each substrate is different, and thus a different nanoporous morphology ensues. This mechanism also explains the general similarity of the morphologies of ITO glass to Si when one considers their relatively similar roughness, at least compared to that of FTO glass.

3.2 Anodized film characterization

A study of the stoichiometry and crystalline phases present after anodization and the subsequent annealing step was conducted through use of XRD and XPS; XRD results are shown in Fig. 2 while XPS results are shown in Fig. 3 and Fig. S3 for the Ni 2p and O 1s spectra respectively. XPS was not conducted on Si samples, but since the annealing temperatures were identical for FTO and Si samples, the spectra corresponding to FTO can be considered representative for Si as the approximately 10 nm surface depth characterized by XPS is not expected to be affected by the underlying substrate. On all substrates after anodizing but before annealing, no crystalline phases are present with the exception of trace amounts of Ni and the substrate. XPS spectra reveal that the films are comprised of amorphous NiOOH and $Ni(OH)_2$ prior to the annealing step; this agrees with prior reports on the anodization of Ni [26]. However, after annealing the film at 600 °C, XRD confirms the formation of crystalline NiO on both FTO and Si samples. On the other hand, NiO peaks on the ITO sample annealed at 375 °C are very weak and the XRD signal was overwhelmed by stronger Ni peaks

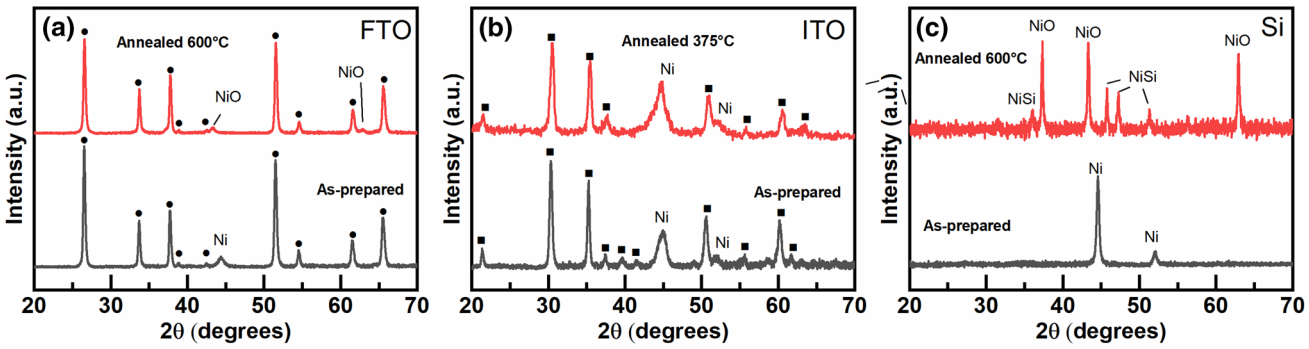

Fig. 2 X-ray diffraction spectra of anodized Ni films on **a** FTO Glass, **b** ITO glass and **c** Si wafer substrates. The top red curve corresponds to annealed samples (600 °C for FTO and Si, 375 °C for ITO), while the bottom right curve corresponds to samples as-prepared after anodizing. The peaks labelled with a black circle corresponds to FTO, while peaks labelled with a black square corresponds to ITO as determined by comparison to works by Yousif et al and Irwin et al respectively [58]. The XRD peak corresponding to the Si substrate, located at $2\theta = 70°$ is just out of frame

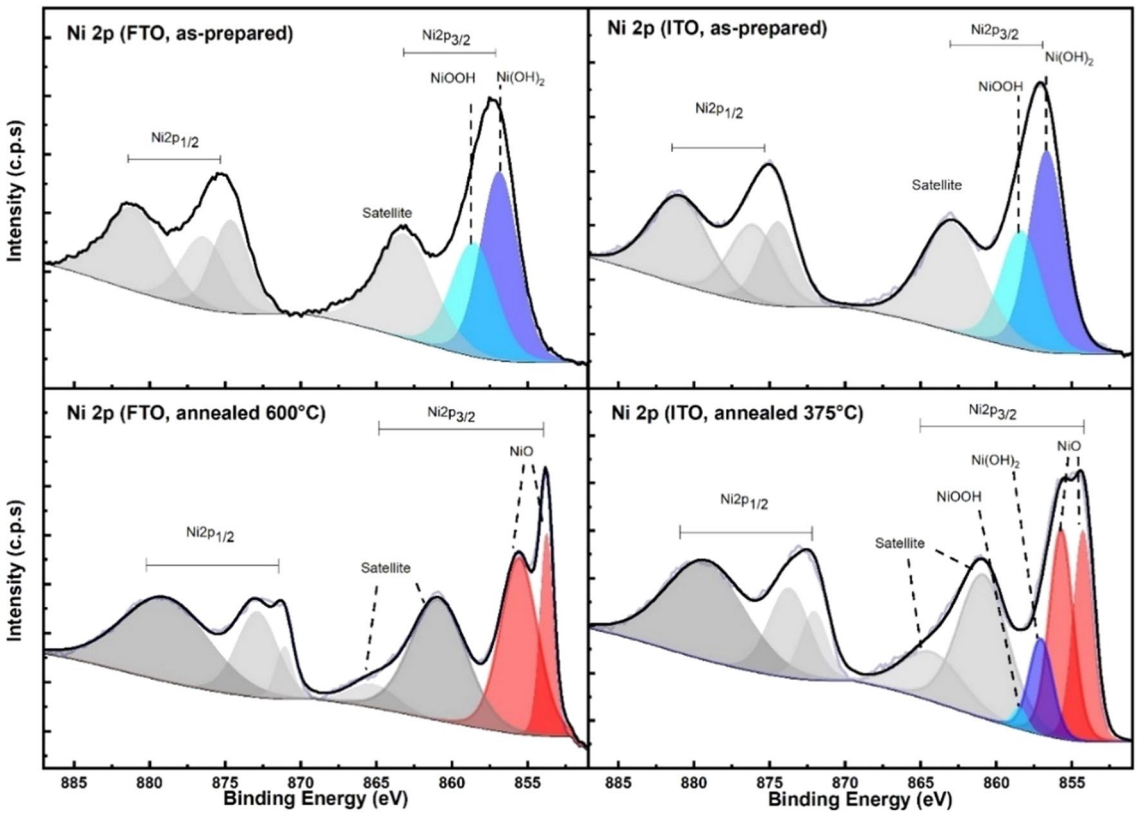

Fig. 3 XPS spectra showing the Ni 2p region of anodized Ni films on **(a)** FTO samples as-prepared, **(b)** ITO samples as-prepared, **(c)** FTO samples annealed 600 °C, **(d)** ITO samples annealed 375 °C

because the annealing temperature was not high enough. XPS results further substantiate this, as significant $Ni(OH)_2$ and NiOOH contributions to the spectra are apparent. This lower annealing temperature was selected in the case of ITO samples because ITO experiences thermal degradation as oxygen diffuses throughout its structure, lowering its conductivity [44]. Thus, 375 °C was the highest temperature that was attempted; clearly, there is incompatibility with a procedure that requires a post-annealing process and the use of ITO. On the other hand, XRD results of annealed NiO/Si samples show the presence of not merely NiO but NiSi as well; from SEM images, this NiSi layer may be estimated to be *ca.*120 nm thick. Comparing the XRD spectra of Si samples before and after annealing, it can be ascertained

that NiSi formed as Ni diffused into Si during the annealing process, a well understood interaction that occurs between the two elements [50]. The formation of NiSi here is unavoidable as NiSi has a much lower formation temperature than NiO, with the onset of formation at ~ 350 °C. However, we also note that NiSi has been investigated extensively for use in the microelectronics industry, such as a contact material for Si-based transistors owing to its low resistivity, and relatively low consumption of silicon during formation [26, 50, 51]. While we do not further investigate the NiO/NiSi/Si structure that forms, it may prove advantageous in device applications.

3.3 Optoelectronic characterization of NiO on FTO-coated glass

The remainder of this work is devoted to optoelectronic investigation of the nanoporous NiO that was synthesized on FTO-coated glass through UV–Vis spectroscopy, electrochemical impedance spectroscopy (EIS) and Mott–Schottky analysis.

As shown in Fig. 4, UV–Vis absorption spectra clearly show the transparency of the NiO at visible wavelengths, which is expected given its large bandgap. In addition, a Tauc plot could be generated in order to determine the optical band gap of the material by plotting $(\alpha hv)^{1/n}$ versus hv, where α is the absorption coefficient, h is Planck's constant, v is the frequency of light, and n is a constant dependent on the electronic transition type (in most cases either direct or indirect transitions are considered, corresponding to an n of ½ or 2 respectively). Here, NiO is assumed to have a direct band gap as has been generally done in the previous literature [52–54]. By extrapolating the linear region of Tauc plot to the point on the y-axis where $(\alpha hv)^{1/2} = 0$, the bandgap was determined to be 3.5 eV, which falls within the range of values typically reported for NiO (3.4–4.0 eV).

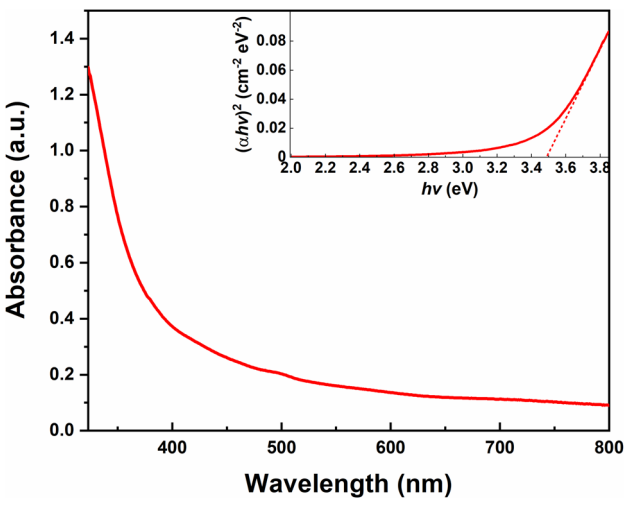

Fig. 4 UV–Vis spectrum of NiO films on FTO-coated glass. The inset shows the Tauc plot of the associated spectrum, with the dashed line showing the measured band gap of the material at the x-intercept

EIS was used to study the semiconductor-electrolyte interfacial behavior of the nanoporous NiO film in a phosphate buffer solution at pH 7, at room temperature and under room lighting conditions. Experimental and fitted Nyquist and Bode Phase plots in the 1–70,000 Hz frequency range under dark condition (i.e. without exposure to illumination), and at an applied potential of − 0.4 V versus Ag/AgCl are shown in Fig. 5a and b. The equivalent circuit of the EIS data is shown in Fig. 5c, where R_S, R_T, R_C, C_{SC}, and C_H are the electrolyte resistance, charge transport resistance, charge transfer resistance, space charge capacitance, and electrochemical double-layer capacitance, respectively. Also present in the equivalent circuit diagram are two constant phase elements (CPEs) denoted by Q_1 and Q_2 with coefficients n_1 and n_2. While impedances due to resistance R_S, R_C, are R_T are frequency independent and have the same magnitude as the resistances themselves, impedances due to capacitances ($Z_{C_{SC}}$ and Z_{C_H}) and constant phase elements (Z_{Q_1} and Z_{Q_2}) are frequency dependent, and are given by Eqs. (1, 2, 3, 4), where $i = \sqrt{-1}$. The total impedance of the system (Z) is given by Eq. (5).

$$Z_{C_{SC}} = \frac{1}{i(2\pi f)C_{SC}} \tag{1}$$

$$Z_{C_H} = \frac{1}{i(2\pi f)C_H} \tag{2}$$

$$Z_{Q_1} = \frac{1}{(i2\pi f)^{n_1}Q_1} \tag{3}$$

$$Z_{Q_2} = \frac{1}{(i2\pi f)^{n_2}Q_2} \tag{4}$$

$$Z = R_S + R_C + R_{CT} + Z_{C_{SC}} + Z_{C_H} + Z_{Q_1} + Z_{Q_2} \tag{5}$$

The values of the equivalent circuit elements were obtained by fitting the transverse function, which was obtained by summing up the impedance of the elements. R_S, R_C and R_T were determined to be 40, 15 and 78 Ω cm^{-2} respectively. Similarly, C_{SC}, and C_H were determined to be 4.2×10^{-8} F cm^{-2} and 6.0×10^{-6} F cm^{-2} respectively. Q_1 and Q_2 were 9.3×10^{-5} F cm^{-2} s$^{-0.19}$ and 2.0×10^{-4} Fcm^{-2}s$^{-0.08}$, respectively, and imply capacitive nature of the constant phase elements. Lastly, n_1 and n_2 were determined to be 0.92 and 0.81 respectively. R_C for this porous NiO film was found to be higher than other porous nickel oxide electrodes and therefore implies reasonable chemical stability [52]. The product of R_T and C_{SC} is the hole-lifetime, τ, which is 3.28 µs.

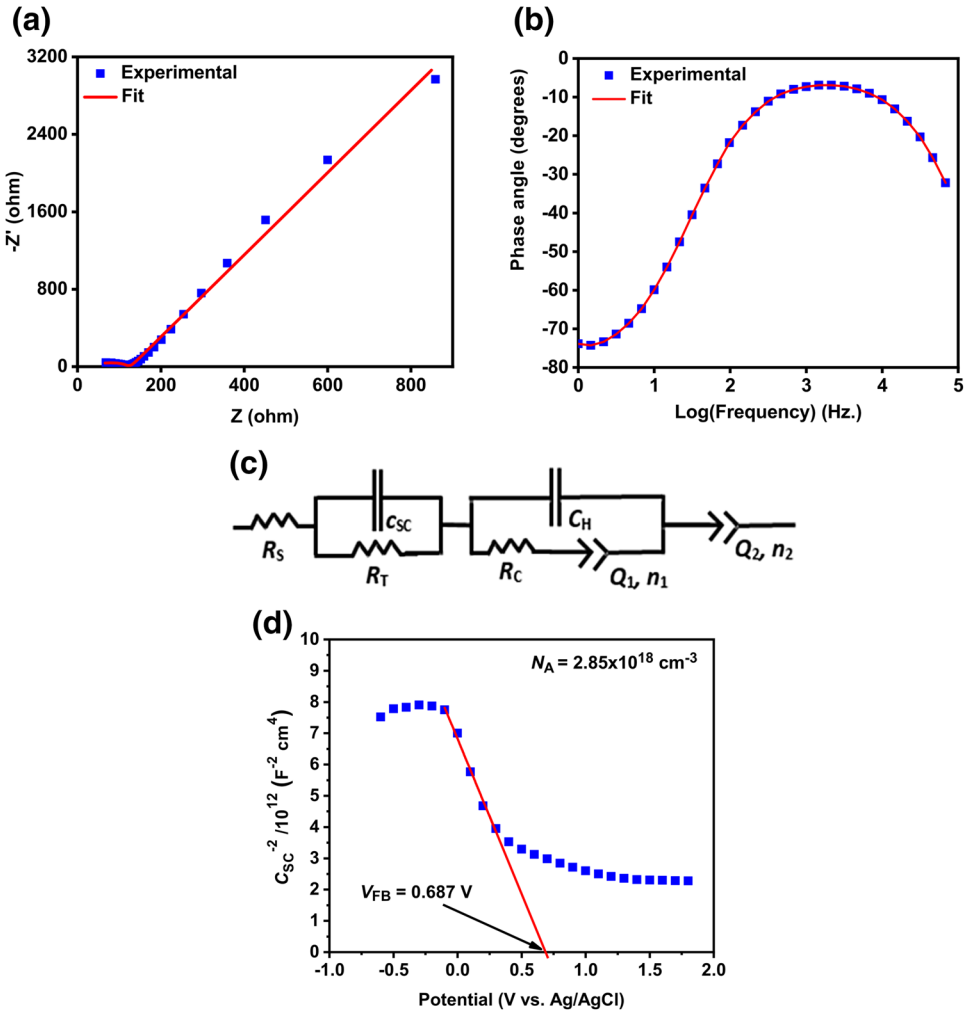

Fig. 5 **a** Nyquist plot, **b** Bode phase plot of the NiO film on FTO. **c** Equivalent circuit representing the Nyquist and Bode plots in **a** and **b**. **d** Mott–Schottky plot of the NiO film showing the V_{FB} and straight-line fit that was used to calculate V_{FB} and N_A

$$\frac{1}{C_{sc}^2} = \frac{2}{e\varepsilon_0\varepsilon_r N_D}\left(V - V_{FB} - \frac{kT}{e}\right) \tag{6}$$

$$N_A = \frac{-2}{e\varepsilon_0\varepsilon_r}\frac{dV}{dC_{SC}^2} \tag{7}$$

Mott–Schottky analysis was performed to estimate the charge carrier concentration (N_A) and flat band potential (V_{FB}) of the nanoporous NiO film on FTO-coated glass; the relevant equations for this analysis are shown in Eq. (6) and (7). In these equations, e is the elementary charge (1.602×10^{-19} °C), ε_0 is the vacuum permittivity (8.854×10^{-12} F m^{-1}), ε_r is the semiconductor dielectric constant, taken as 5 for NiO [55], V is the applied potential, k is the Boltzmann constant (1.381×10^{-23} J K^{-1}), and T is the absolute temperature in K. N_A was calculated using Eq. (7) and the slope of the Mott–Schottky's plot (Fig. 5d). The slope is noted to be negative, which confirms the expected p-type behaviour. N_A is found to be 2.85×10^{18} cm^{-3}, a value that is similar to acceptor densities values reported in literature [56, 57]. V_{FB} was determined from the intersection of the slope of the Mott–Schottky plot with the horizontal axis denoting potential, and was found to be 0.687 V versus Ag/AgCl.

4 Conclusion

We have presented, for the first time, anodized nanoporous NiO on non-native substrates. The formed NiO layers on FTO:glass and ITO:glass were approximately 200 nm thick. An approximately 120 nm thick layer of NiSi is present underneath anodized NiO on Si wafers. It should be noted that since NiO is more vulnerable to etching processes than other valve metals that have been successfully anodized to their oxides (such as Al and Ti), precise control of synthesis conditions is required. This is doubly true when anodizing thin films of Ni—as there is no bulk amount of Ni below the anodized layer, there is little leeway in the anodizing process, and removal of the film may occur very suddenly. We found that using a constant current when anodizing at ice bath temperatures helped prevent overetching from occurring and resulted in a more nanoporous morphology.

A diethylene glycol-based electrolyte was found to result in pores an order of magnitude larger that ethylene glycol-based electrolytes. We also found that anodized NiO demonstrated an appropriate bandgap and charge carrier densities of 3.5 eV and 2.85×10^{18} cm^{-3} respectively, indicating that the quality of the nanoporous layer is excellent.

Acknowledgements This work was supported by funding from CMC Microsystems, Natural Sciences and Engineering Research Council of Canada (NSERC), and Future Energy Systems. R.K. would like to thank NSERC for scholarship support. R.K. and U.K.T. would like to thank Alberta Innovates for scholarship support.

Compliance with ethical standards

Conflicts of interest The authors have no conflicts of interest to declare.

References

1. S. Rühle, A.Y. Anderson, H.-N. Barad, B. Kupfer, Y. Bouhadana, E. Rosh-Hodesh, A. Zaban, J. Phys. Chem. Lett. **3**, 3755 (2012). https://doi.org/10.1021/jz3017039
2. Z. Wang, P.K. Nayak, J.A. Caraveo-Frescas, H.N. Alshareef, Adv. Mater. **28**, 3831 (2016). https://doi.org/10.1002/adma.201503080
3. P.M. Rao, L. Cai, C. Liu, I.S. Cho, C.H. Lee, J.M. Weisse, P. Yang, X. Zheng, Nano Lett. **14**, 1099 (2014)
4. P. Kar, K. Shankar, J. Nanosci. Nanotechnol. **13**, 4473 (2013). https://doi.org/10.1166/jnn.2013.7771
5. M.H. Zarifi, S. Farsinezhad, M. Abdolrazzaghi, M. Daneshmand, K. Shankar, Nanoscale (2016). https://doi.org/10.1039/c5nr06567d
6. D. Sarkar, S. Ishchuk, D.H. Taffa, N. Kaynan, B.A. Berke, T. Bendikov, R. Yerushalmi, J. Phys. Chem. C **120**, 3853 (2016). https://doi.org/10.1021/acs.jpcc.5b11795
7. Y. Wang, L. Zhu, T. Wang, Y. Hu, Z. Deng, Q. Cui, Z. Lou, Y. Hou, F. Teng, Org. Electron. **59**, 63 (2018). https://doi.org/10.1016/j.orgel.2018.04.033
8. G. Katwal, M. Paulose, I.A. Rusakova, J.E. Martinez, O.K. Varghese, Nano Lett. **16**, 3014 (2016). https://doi.org/10.1021/acs.nanolett.5b05280
9. M.I.A. Umar, F.Y. Naumar, M.M. Salleh, A.A. Umar, J. Mater. Sci.: Mater. Electron. **29**, 6892 (2018). https://doi.org/10.1007/s10854-018-8675-2
10. P. Kar, Y. Zhang, S. Farsinezhad, A. Mohammadpour, B.D. Wiltshire, H. Sharma, K. Shankar, Chem. Commun. **51**, 7816 (2015). https://doi.org/10.1039/C5CC01829C
11. U.K. Thakur, A.M. Askar, R. Kisslinger, B.D. Wiltshire, P. Kar, K. Shankar, Nanotechnology **28**, 274001 (2017)
12. D.-D. Qin, C.-L. Tao, S.-I. In, Z.-Y. Yang, T.-E. Mallouk, N. Bao, C.A. Grimes, Energy Fuels **25**, 5257 (2011). https://doi.org/10.1021/ef201367q
13. T.J. LaTempa, X. Feng, M. Paulose, C.A. Grimes, J. Phys. Chem. C **113**, 16293 (2009). https://doi.org/10.1021/jp904560n
14. N.K. Allam, X.J. Feng, C.A. Grimes, Chem. Mater. **20**, 6477 (2008). https://doi.org/10.1021/cm801472y
15. M.M. Momeni, M. Mirhosseini, M. Chavoshi, Ceram. Int. **42**, 9133 (2016)
16. Y. Alivov, V. Singh, Y. Ding, P. Nagpal, Nanotechnology **25**, 385202 (2014)
17. J.-S. Baik, G. Yun, M. Balamurugan, S.K. Lee, J.-H. Kim, K.-S. Ahn, S.H. Kang, J. Electrochem. Soc. **163**, H1165 (2016). https://doi.org/10.1149/2.1091614jes
18. J. He, Y. Hu, Z. Wang, W. Lu, S. Yang, G. Wu, Y. Wang, S. Wang, H. Gu, J. Wang, J. Mater. Chem. C **2**, 8185 (2014). https://doi.org/10.1039/C4TC01581A
19. C.W. Lai, S.B. Abd Hamid, S. Sreekantan, Int. J. Photoenergy **2013**, 6 (2013). https://doi.org/10.1155/2013/745301
20. J.-H. Ha, P. Muralidharan, D.K. Kim, J. Alloys Compd. **475**, 446 (2009). https://doi.org/10.1016/j.jallcom.2008.07.048
21. C.E. Castillo, M. Gennari, T. Stoll, J. Fortage, A. Deronzier, M.N. Collomb, M. Sandroni, F. Légalité, E. Blart, Y. Pellegrin, C. Delacote, M. Boujtita, F. Odobel, P. Rannou, S. Sadki, J. Phys. Chem. C **119**, 5806 (2015). https://doi.org/10.1021/jp511469f
22. Z. Zhu, Y. Bai, T. Zhang, Z. Liu, X. Long, Z. Wei, Z. Wang, L. Zhang, J. Wang, F. Yan, S. Yang, Angew. Chem. **126**, 12779 (2014). https://doi.org/10.1002/ange.201405176
23. S.R. Nalage, M.A. Chougule, S. Sen, P.B. Joshi, V.B. Patil, Thin Solid Films **520**, 4835 (2012). https://doi.org/10.1016/j.tsf.2012.02.072
24. B.R. Cruz-Ortiz, M.A. Garcia-Lobato, E.R. Larios-Durán, E.M. Múzquiz-Ramos, J.C. Ballesteros-Pacheco, J. Electroanal. Chem. **772**, 38 (2016). https://doi.org/10.1016/j.jelechem.2016.04.020
25. A. Sápi, A. Varga, G.F. Samu, D. Dobó, K.L. Juhász, B. Takács, E. Varga, Á. Kukovecz, Z. Kónya, C. Janáky, J. Phys. Chem. C **121**, 12148 (2017). https://doi.org/10.1021/acs.jpcc.7b00429
26. C. Hu, K. Chu, Y. Zhao, W.Y. Teoh, ACS Appl. Mater. Inter. **6**, 18558 (2014). https://doi.org/10.1021/am507138b
27. J. Bandara, K. Shankar, J. Basham, H. Wietasch, M. Paulose, O.K. Varghese, C.A. Grimes, M. Thelakkat, Eur. Phys. J. Appl. Phys. **53**, 20601 (2011). https://doi.org/10.1051/epjap/2010100387
28. V. Galstyan, A. Vomiero, E. Comini, G. Faglia, G. Sberveglieri, RSC Adv. **1**, 1038 (2011). https://doi.org/10.1039/c1ra00077b
29. V. Galstyan, A. Vomiero, I. Concina, A. Braga, M. Brisotto, E. Bontempi, G. Faglia, G. Sberveglieri, Small **7**, 2437 (2011). https://doi.org/10.1002/smll.201101356
30. S.L. Lim, Y.L. Liu, J. Li, E.T. Kang, C.K. Ong, Appl. Surf. Sci. **257**, 6612 (2011). https://doi.org/10.1016/j.apsusc.2011.02.087
31. J. Weickert, C. Palumbiny, M. Nedelcu, T. Bein, L. Schmidt-Mende, Chem. Mater. **23**, 155 (2011). https://doi.org/10.1021/cm102389m
32. T. Yuxin, T. Jie, D. Zhili, O. Joo Tien, C. Zhong, Adv. Nat. Sci.: Nanosci. Nanotechnol. **2**, 045002 (2011)
33. K.N. Chappanda, Y.R. Smith, M. Misra, S.K. Mohanty, Nanotechnology (2012). https://doi.org/10.1088/0957-4484/23/38/385601
34. K.N. Chappanda, Y.R. Smith, S.K. Mohanty, L.W. Rieth, P. Tathireddy, M. Misra, Nanoscale Res. Lett. (2012). https://doi.org/10.1186/1556-276x-7-388
35. M Okada, K Tajima, Y Yamada, K Yoshimura (2012) In Pan F, Chen X (eds)18th International Vacuum Congress
36. J. Tupala, M. Kemell, E. Harkonen, M. Ritala, M. Leskela, Nanotechnology (2012). https://doi.org/10.1088/0957-4484/23/12/125707
37. H. Wang, H.Y. Li, J.S. Wang, J.S. Wu, Mater. Lett. **80**, 99 (2012). https://doi.org/10.1016/j.matlet.2012.04.053
38. S. Farsinezhad, A. Mohammadpour, A.N. Dalrymple, J. Geisinger, P. Kar, M.J. Brett, K. Shankar, J. Nanosci. Nanotechnol. **13**, 2885 (2013). https://doi.org/10.1166/jnn.2013.7409
39. S. Farsinezhad, A.N. Dalrymple, K. Shankar, Phys. Status Solidi A **211**, 1113 (2014). https://doi.org/10.1002/pssa.201330649
40. K.N. Chappanda, Y.R. Smith, L.W. Rieth, P. Tathireddy, M. Misra, S.K. Mohanty, IEEE T. Nanotechnol. **14**, 18 (2015). https://doi.org/10.1109/TNANO.2014.2360501
41. S. Farsinezhad, A. Mohammadpour, M. Benlamri, A.N. Dalrymple, K. Shankar, J. Nanosci. Nanotechnol. **17**, 4936 (2017). https://doi.org/10.1166/jnn.2017.13310

42. J.A. Thornton, J. Vac. Sci. Technol. **11**, 666 (1974). https://doi.org/10.1116/1.1312732
43. T.H. Choudhury, S. Raghavan, Scr. Mater. **105**, 18 (2015). https://doi.org/10.1016/j.scriptamat.2015.04.017
44. M. Paulose, K. Shankar, S. Yoriya, H.E. Prakasam, O.K. Varghese, G.K. Mor, T.A. Latempa, A. Fitzgerald, C.A. Grimes, J. Phys. Chem. B **110**, 16179 (2006). https://doi.org/10.1021/jp064020k
45. S. Yoriya, C.A. Grimes, Langmuir **26**, 417 (2010). https://doi.org/10.1021/la9020146
46. S.P. Albu, P. Schmuki, Physica Status Solidi RRL **4**, 215 (2010). https://doi.org/10.1002/pssr.201004244
47. A. Mohammadpour, P.R. Waghmare, S.K. Mitra, K. Shankar, ACS Nano **4**, 7421 (2010). https://doi.org/10.1021/nn1026214
48. D. Kowalski, J. Mallet, J. Michel, M. Molinari, J. Mater. Chem. A **3**, 6655 (2015). https://doi.org/10.1039/C4TA06714B
49. X. Zhong, D. Yu, Y. Song, D. Li, H. Xiao, C. Yang, L. Lu, W. Ma, X. Zhu, Mater. Res. Bull. **60**, 348 (2014). https://doi.org/10.1016/j.materresbull.2014.09.011
50. A. Mohammadpour, K. Shankar, J. Mater. Chem. **20**, 8474 (2010). https://doi.org/10.1039/C0JM02198A
51. Y.-N. Kim, H.-G. Shin, J.-K. Song, D.-H. Cho, H.-S. Lee, Y.-G. Jung, J. Mater. Res. **20**, 1574 (2005). https://doi.org/10.1557/JMR.2005.0199
52. M.D. Irwin, D.B. Buchholz, A.W. Hains, R.P.H. Chang, T.J. Marks, Proc. Natl. Acad. Sci. USA **105**, 2783 (2008)
53. F.A. Geenen, E. Solano, J. Jordan-Sweet, C. Lavoie, C. Mocuta, C. Detavernier, J. Appl. Phys. **123**, 185302 (2018). https://doi.org/10.1063/1.5022070
54. S.A. Yousif, J.M. Abass, Int. Lett. Chem. Phys. Astron. **18**, 90 (2013). https://doi.org/10.18052/www.scipress.com/ILCPA.18.90
55. L. Ai, G. Fang, L. Yuan, N. Liu, M. Wang, C. Li, Q. Zhang, J. Li, X. Zhao, Appl. Surf. Sci. **254**, 2401 (2008). https://doi.org/10.1016/j.apsusc.2007.09.051
56. N.M. Hosny, Polyhedron **30**, 470 (2011). https://doi.org/10.1016/j.poly.2010.11.020
57. N. Park, K. Sun, Z. Sun, Y. Jing, D. Wang, J. Mater. Chem. C **1**, 7333 (2013). https://doi.org/10.1039/C3TC31444H
58. C. Lavoie, F.M. d'Heurle, C. Detavernier, C. Cabral, Microelectron. Eng. **70**, 144 (2003). https://doi.org/10.1016/S0167-9317(03)00380-0

Supplementary Information

Transparent Nanoporous P-type NiO Films Grown Directly on Non-Native Substrates by Anodization

Ryan Kisslinger,[a] Saralyn Riddell,[a] Spencer Savela,[a] Piyush Kar,[a] Ujwal K. Thakur,[a] Sheng Zeng[a] and Karthik Shankar[a]

[a]*Department of Electrical and Computer Engineering, University of Alberta, 9211 - 116 St, Edmonton, Alberta, Canada T6G 1H9*

***Authors to whom correspondence should be addressed:**

1. Karthik Shankar (kshankar@ualberta.ca)
2. Ryan Kisslinger (kissling@ualberta.ca)

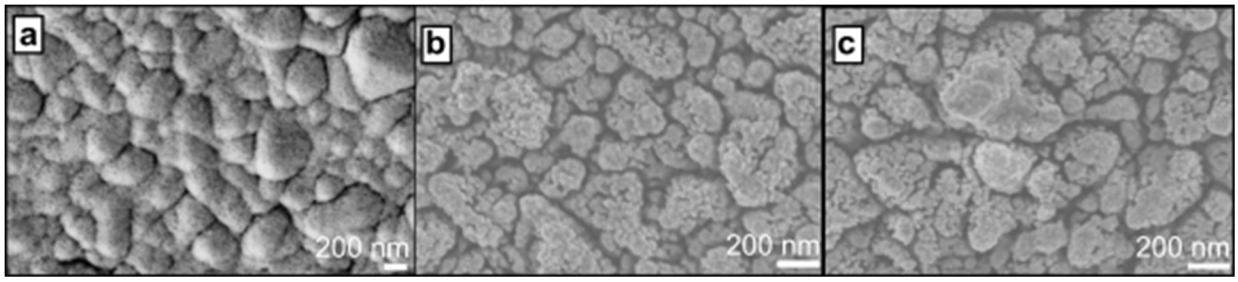

Figure S1. SEM images of anodized Ni films on FTO Glass, following the standard optimized recipe with the following exception as noted: (a) using ethylene glycol in place of diethylene glycol (b) anodization was begun with electrolyte at room temperature instead of chilled in ice bath (c) anodization conducted at constant voltage of 45 V. All scale bars correspond to 200 nm.

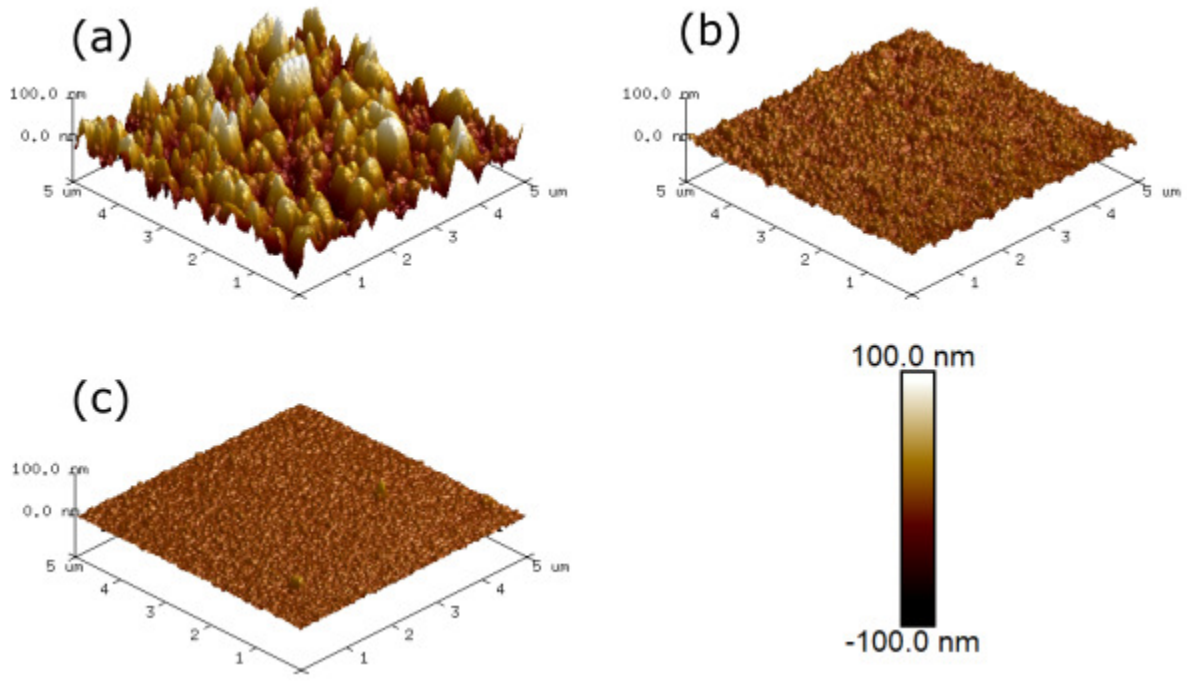

Figure S2. Three-dimensional AFM Images of sputtered Ni on (a) FTO Glass, (b) ITO Glass, and (c) a silicon wafer. Shown in the bottom right corner of the figure is the scale for interpreting topographical heights by colour.

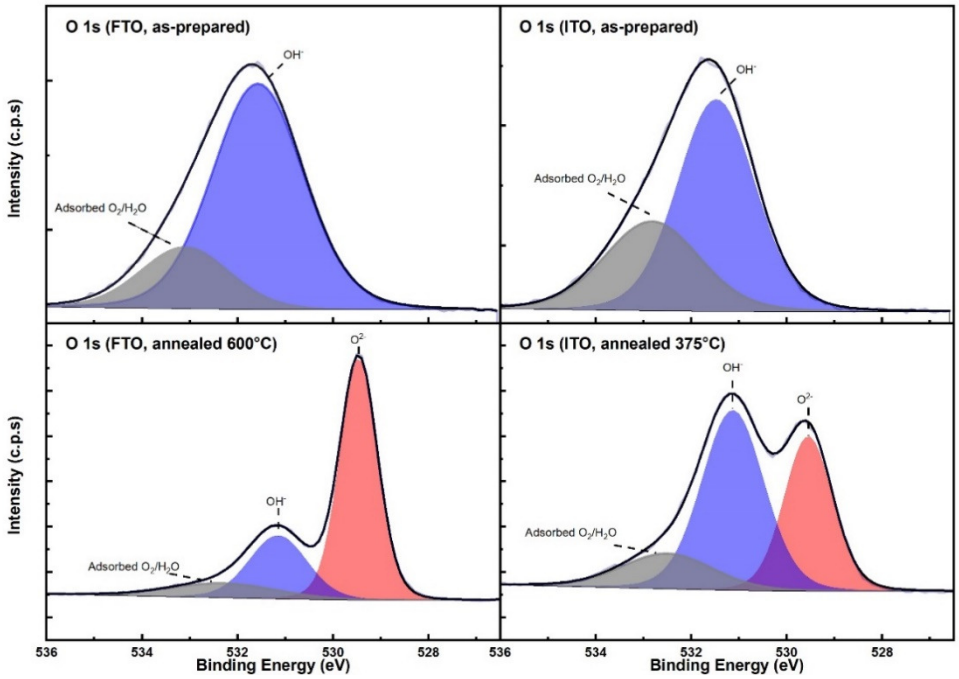

Figure S3. XPS spectra showing the O 1s region of anodized Ni films on (a) FTO samples as-prepared, (b) ITO samples as-prepared, (c) FTO samples annealed 600°C, (d) ITO samples annealed 375°C.